

Numerical study on fast particle confinement in Chinese first quasi-axisymmetric stellarator

Yi-Hang Shou(寿毅航), Xian-Qu Wang(王先驱), Zhi-Ru Li(李志儒), Yu-Cai Li(栗钰彩), Yu-Hong Xu(许宇鸿), Jun Cheng(程钧), Hai-Feng Liu(刘海峰), Jie Huang(黄捷), Xin Zhang(张欣), Hai Liu(刘海), Jun-Feng Shen(沈军峰), Jun Hu(胡军), and Chang-Jian Tang(唐昌建)

Citation: Chin. Phys. B, 2026, 35 (**3**): 035204. DOI: 10.1088/1674-1056/adf828
http://cpb.iphy.ac.cn; http://iopscience.iop.org/cpb

What follows is a list of articles you may be interested in

Effect of the relative phase between pre-existing 2/1 and 3/1 magnetic islands on the suppression of runaway electrons on J-TEXT

Jin-Yu Xiong(熊金玉), Zhong-He Jiang(江中和), Zi-Xiao Jiao(焦子啸), Zhen Li(李振),Yun-Feng Liang(梁云峰), Zhong-Yong Chen(陈忠勇), Yong-Hua Ding(丁永华), and J-TEXT Team
Chin. Phys. B, 2023, 32 (**7**): 075210. DOI: 10.1088/1674-1056/acc3f9

Effect of tearing modes on the confinement of runaway electrons in Experimental Advanced Superconducting Tokamak

Rui-Jie Zhou(周瑞杰)
Chin. Phys. B, 2023, 32 (**7**): 075204. DOI: 10.1088/1674-1056/acc3f8

Electron acceleration during magnetic islands coalescence and division process in a guide field reconnection

Shengxing Han(韩圣星), Huanyu Wang(王焕宇), and Xinliang Gao(高新亮)
Chin. Phys. B, 2022, 31 (**2**): 025202. DOI: 10.1088/1674-1056/ac21c0

Numerical study of fast ion behavior in the presence of magnetic islands and toroidal field ripple in the EAST tokamak

Zhang Wei (张伟), Hu Li-Qun (胡立群), Sun You-Wen (孙有文), Ding Si-Ye (丁斯晔), Zhang Zi-Jun (张子君), Liu Song-Lin (刘松林)
Chin. Phys. B, 2014, 23 (**10**): 105201. DOI: 10.1088/1674-1056/23/10/105201

Numerical study on fast particle confinement in Chinese first quasi-axisymmetric stellarator

Yi-Hang Shou(寿毅航)[1], Xian-Qu Wang(王先驱)[1,†], Zhi-Ru Li(李志儒)[1], Yu-Cai Li(栗钰彩)[1], Yu-Hong Xu(许宇鸿)[1], Jun Cheng(程钧)[1], Hai-Feng Liu(刘海峰)[1], Jie Huang(黄捷)[1], Xin Zhang(张欣)[1], Hai Liu(刘海)[1], Jun-Feng Shen(沈军峰)[1], Jun Hu(胡军)[1], and Chang-Jian Tang(唐昌建)[2]

[1] *Institute of Fusion Science, School of Physical Science and Technology, Southwest Jiaotong University, Chengdu* 610031, *China*
[2] *School of Physical Science and Technology, Sichuan University, Chengdu* 610041, *China*

(Received 18 April 2025; revised manuscript received 28 July 2025; accepted manuscript online 6 August 2025)

Fast particle confinement in the Chinese first quasi-axisymmetric stellarator (CFQS) is investigated using the MEGA code, comparing the standard quasi-axisymmetric (QA) configuration with a finite-beta ($\langle\beta\rangle = 0.74\%$) equilibrium featuring magnetic islands. In the standard QA configuration, the drift associated with the vertical magnetic curvature term, $(\nabla\times\boldsymbol{b})_z$, is identified as the dominant loss mechanism, especially for co-passing particles. In the finite-beta configuration, magnetic islands trap low-energy particles. The $(\nabla\times\boldsymbol{b})_z$ drift modulates this trapping, promoting escape for co-passing particles while reinforcing trapping for counter-passing particles, and remains a significant contributor to overall losses. These findings underscore the critical role of the $(\nabla\times\boldsymbol{b})_z$ drift and the added complexities of magnetic islands for energetic particle confinement in finite-beta stellarator plasmas.

Keywords: quasi-axisymmetric stellarator, fast particle, particle confinement, CFQS, magnetic islands

PACS: 52.55.Hc, 52.55.Dy, 52.55.–s, 28.52.–s

DOI: 10.1088/1674-1056/adf828 **CSTR:** 32038.14.CPB.adf828

1. Introduction

Magnetic confinement reactors must effectively confine the fast particles generated from fusion reactions. Enhancing the confinement of fast particles contributes to improving the heating efficiency of the bulk plasma. The study of fast particle confinement is one of the critical topics in the physics research of tokamaks and stellarators. In optimized stellarators, the quasi-axisymmetric (QA) stellarator combines the advantages of tokamak and traditional stellarator with a magnetic configuration not requiring current drive and reducing the neoclassical transport.[1,2]

The potential advantages of quasi-axisymmetric stellarator in plasma confinement have widely been explored internationally by studying the physical and engineering design of quasi-axisymmetric stellarator at various research centers, including the Compact Helical System (CHS)-qa,[3–5] National Compact Stellarator Experiment (NCSX).[6–9] Recently, a new QA device consisting of Chinese first quasi-axisymmetric stellarator (CFQS) is jointly developed by the Southwest Jiaotong University (SWJTU) and the National Institute for Fusion Science (NIFS) to research key scientific issues, such as turbulent transport and MHD instabilities to improve the stellarator confinement performance. The basic parameters of the CFQS device consist of a major radius of 1 m (with a toroidal periodicity of 2), a magnetic field strength of 1 T, and a minor radius of 0.25 m.[10–17]

In previous studies, particle orbits in stellarators are broadly classified as either passing or trapped. Trapped particles, which are reflected by regions of high magnetic field strength, are further categorized based on the nature of the magnetic well in which they are confined. Particles trapped in the main toroidal variation of the magnetic field are known as toroidally trapped or banana particles. Those trapped in smaller, localized ripples of the magnetic field are termed locally trapped or ripple-trapped particles. A special, often vulnerable, subset of toroidally trapped particles are barely-trapped particles, whose turning points are close to the magnetic field maxima.[18] Su and colleagues used the single-particle orbit model to simulate particle confinement in the CFQS. They identified the confinement regions for trapped particles and analyzed the mechanisms of orbit transitions.[19] Yang *et al.* conducted simulations on the confinement effects of the QA configuration in the CFQS stellarator and proposed a magnetic configuration optimization strategies.[20] While these studies provided crucial baseline understanding for the standard CFQS QA design, assessing the robustness of particle confinement under more challenging, reactor-relevant conditions, such as finite-beta scenarios where magnetic islands can develop, remains an important task.

To further evaluate the fast particle confinement performance within the CFQS device under different operational conditions, this study utilizes the MEGA code for numeri-

†Corresponding author. E-mail: xianquwang@swjtu.edu.cn

© 2026 Chinese Physical Society and IOP Publishing Ltd. All rights, including for text and data mining, AI training, and similar technologies, are reserved.

cal simulations. We specifically investigate the behavior and confinement characteristics of fast particles in two distinct magnetic configurations: (i) the standard quasi-axisymmetric (QA) configuration of CFQS, and (ii) a finite-beta equilibrium ($\langle\beta\rangle = 0.74\%$) which features prominent magnetic islands. Understanding how these magnetic islands, potentially present at higher beta values, affect particle orbits and losses is critical for predicting CFQS performance. After introducing the MEGA code and simulation setup in Section 2, Section 3 presents the analysis of the particle trajectories, confinement properties (*e.g.*, loss fractions), and loss mechanisms observed in both the standard QA and the finite-beta island configurations. Section 4 summarizes the key findings and conclusions.

2. Model and equations

The MEGA code uses a hybrid simulation model for MHD and energetic particles.[21–23] The bulk plasma is described by the nonlinear full MHD equations. Fast particles' motion is simulated using drift kinetic equations with the δf particle-in-cell method.[24,25] For the specific scope of this study, MEGA is utilized in a simpler, yet powerful, test-particle mode. We focus on tracing the guiding-center orbits of fast particles within static, pre-calculated three-dimensional (3D) magnetic equilibrium fields obtained from the HINT code. In this mode, the guiding-center velocity $\boldsymbol{u}$ is calculated as

$$\boldsymbol{u} = \boldsymbol{v}_{\parallel}^{*} + \boldsymbol{v}_E + \boldsymbol{v}_B, \tag{1}$$

$$\boldsymbol{v}_{\parallel}^{*} = \frac{v_{\parallel}}{B^{*}}\left[\boldsymbol{B} + \rho_{\parallel} B \boldsymbol{\nabla} \times \boldsymbol{b}\right], \tag{2}$$

$$\boldsymbol{v}_E = \frac{1}{B^{*}}[\boldsymbol{E} \times \boldsymbol{b}], \tag{3}$$

$$\boldsymbol{v}_B = \frac{1}{q_{\mathrm{h}} B^{*}}[-\mu \boldsymbol{\nabla} B \times \boldsymbol{b}], \tag{4}$$

$$\rho_{\parallel} = \frac{m_{\mathrm{h}} v_{\parallel}}{q_{\mathrm{h}} B}, \tag{5}$$

$$\boldsymbol{b} = \boldsymbol{B}/B, \tag{6}$$

$$B* = B(1 + \rho_{\parallel} \boldsymbol{b} \cdot \boldsymbol{\nabla} \times \boldsymbol{b}), \tag{7}$$

$$m_{\mathrm{h}} v_{\parallel} \frac{\mathrm{d}v_{\parallel}}{\mathrm{d}t} = \boldsymbol{v}_{\parallel}^{*} \cdot [q_{\mathrm{h}} \boldsymbol{E} - \mu \boldsymbol{\nabla} B]. \tag{8}$$

Here, $v_{\parallel}$ includes the velocity parallel to the magnetic field and the magnetic curvature drift velocity; $\boldsymbol{v}_E$ is the $\boldsymbol{E} \times \boldsymbol{b}$ drift velocity; $\boldsymbol{v}_B$ is the magnetic gradient drift velocity, and q_{h} and μ are the particle charge and magnetic moment. It should be noted that this simulation neglects the collisional effects in the dynamics of fast particles. The reason is that, for high-energy particles in the early confinement phase, the collision time is much longer than the characteristic confinement time. This ensures that only after the particles go through the slowing-down process, collisional scattering into the loss cone becomes significant.[26]

Two distinct 3D magnetic equilibrium configurations for CFQS, both generated using the HINT code,[17,27] are investigated in this study. The HINT code solves the MHD equilibrium equations without assuming nested flux surfaces, making it suitable for configurations that may contain magnetic islands or stochastic regions. The key parameters for both configurations are an on-axis magnetic field strength $B = 1$ T, major radius $R_0 = 1$ m, and minor radius $r = 0.25$ m. The two configurations are given as follows. (i) Standard QA configuration: This represents the baseline quasi-axisymmetric design equilibrium for CFQS, optimized for good neoclassical confinement properties. (ii) Finite-beta island configuration: This equilibrium corresponds to a finite-beta state calculated by HINT with an average $\langle\beta\rangle = 0.74\%$. This configuration exhibits significant $m/n = 4/2$ magnetic islands, which arise self-consistently in the HINT calculation at this beta value.

In the simulation, the velocities used in this paper are normalized by Alfvén velocity $v_{\mathrm{A}} = B/\sqrt{\mu_0 \rho}$. The normalized velocity range $v = 0.5$–1.5 investigated in this study corresponds to an energy range of approximately 60 keV to 500 keV for deuterium ions. A total of 4×10^6 marker fast particles were launched with an initial uniform spatial distribution throughout the entire simulation domain (R, φ, z). This means that at the start of the simulation, particles are loaded both inside and outside the last closed flux surface (LCFS). The number of grid points is $128 \times 256 \times 128$ for the cylindrical coordinates (R, φ, z). The particle loss rate is obtained by counting the number of particles that go outside the last closed flux surface.

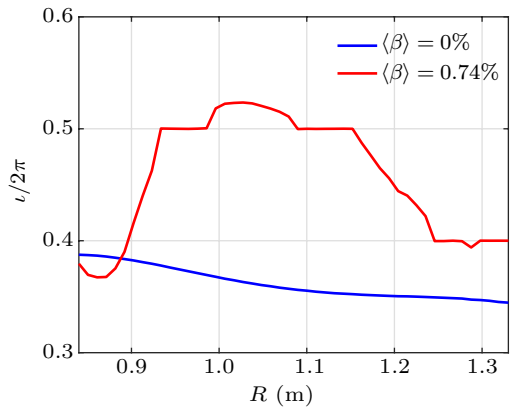


Fig. 1. Rotational transform ($\iota/2\pi$) profiles for standard QA and finite-beta ($\langle\beta\rangle = 0.74\%$) configurations.

3. Simulation results

3.1. Particle orbits in the standard QA configuration

To understand the basic orbit topology within the standard CFQS QA configuration, figure 2 illustrates typical guiding-center trajectories for passing particles projected onto the poloidal plane ($\varphi = \pi/2$). The figure shows orbits with different initial normalized velocities ($v = 0.1$, 0.2, 0.3). Two characteristic pitch angles are shown: co-passing ($\lambda = v_{\parallel}/v = 1$)

and counter-passing ($\lambda = -1$). Consistent with guiding-center drift physics in toroidal devices, the particle trajectories drift from initial magnetic flux surfaces. As shown in Fig. 2, co-passing particles ($\lambda = 1$), whose parallel velocity is in the direction of the magnetic field, experience a net inward radial drift. Conversely, counter-passing particles ($\lambda = -1$), moving opposite to the field direction, exhibit a net outward radial drift. This behavior arises primarily from the vertical drifts (∇B and curvature drifts) combined with the rotational transform of the magnetic field lines. A key observation from Fig. 2 is the dependence of the drift magnitude on particle velocity. The radial drift for both co- and counter-passing particles becomes significantly larger as the normalized velocity increases from 0.1 to 0.3. This clearly demonstrates that higher energy particles experience larger drifts, causing their orbits to deviate more substantially from the magnetic surfaces. This increased drift inherently makes faster particles more susceptible to loss, highlighting the critical challenge of confining fast particles in fusion devices.

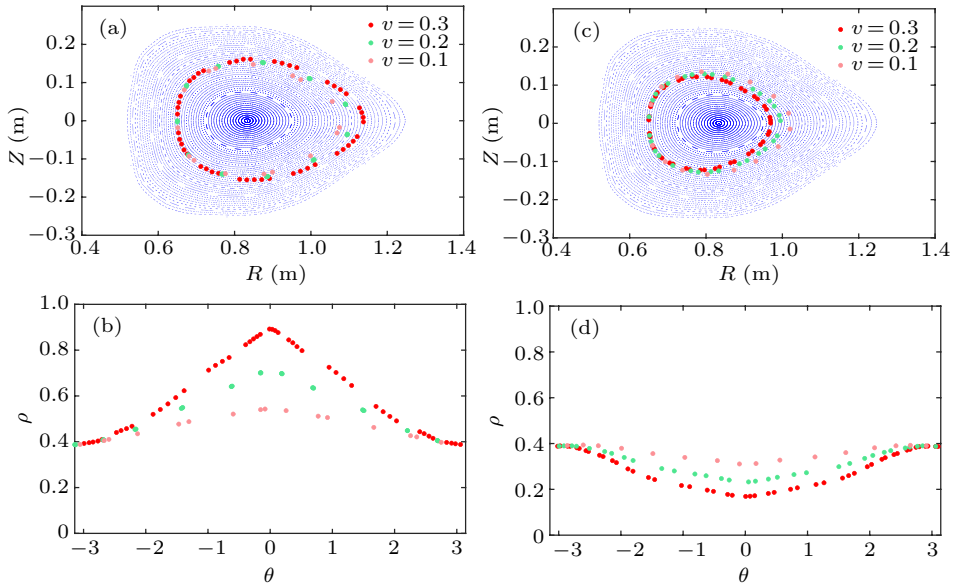


Fig. 2. Particle trajectories at the $\varphi = \pi/2$ section in QA configuration: (a) pitch angle $\lambda = -1$ in R–Z space, (b) pitch angle $\lambda = -1$ in θ–ρ space, (c) pitch angle $\lambda = 1$ in R–Z space, (d) pitch angle $\lambda = 1$ in θ–ρ space.

To clarify the dominant mechanisms driving particle drift and subsequent losses, we performed simulations where key terms in the guiding-center equations (Eqs. (2)–(4)) were selectively deactivated. This allows us to isolate the contribution of different physical effects including $\boldsymbol{E} \times \boldsymbol{B}$, ∇B, and $\nabla \times \boldsymbol{b}$.

Figure 3 illustrates the impact of deactivating specific terms on particle trajectories. It compares trajectories for fast particles with velocity $v = 0.3$. Separate comparisons are shown for (a) a counter-passing ($\lambda = -1$) particle and (b) a co-passing ($\lambda = 1$) particle orbits. It should be noted that for this illustrative figure, the initial radial positions for the co-passing ($\rho \approx 0.4$) and counter-passing ($\rho \approx 0.2$) particles were chosen differently for visual clarity. The counter-passing particle was launched from a more internal position because its strong outward drift at this energy would cause a rapid loss if launched from $\rho \approx 0.4$, which would obscure the visualization of its characteristic drift orbit. The figure clearly demonstrates that deactivating the $(\nabla \times \boldsymbol{b})_z$ term effect significantly suppresses the large radial drifts observed in the full simulation for both co- and counter-passing particles. This strongly indicates that this specific term, arising from the magnetic field curvature in the vertical direction, is the primary driver of the orbit drift.

To quantify the effect of different drift components on overall confinement, we compared the calculated fast particle loss fractions at a specific time ($t = 0.057$ ms) under different conditions: (i) the full equations (initial condition), and after selectively turning off (ii) the entire $\nabla \times \boldsymbol{b}$ term effect, (iii) only the radial component effect $(\nabla \times \boldsymbol{b})_R$, (iv) only the vertical component effect $(\nabla \times \boldsymbol{b})_z$, and (v) only the toroidal component effect $(\nabla \times \boldsymbol{b})_\varphi$.

Table 1 summarizes these loss fractions. The results demonstrate that disabling either the full $\nabla \times \boldsymbol{b}$ term effect or, consistent with the trajectory analysis in Fig. 3, disabling just its vertical component effect $(\nabla \times \boldsymbol{b})_z$ leads to a significant reduction in the loss fraction for fast particles compared to the simulation with all terms active. Conversely, deactivating only the radial $(\nabla \times \boldsymbol{b})_R$ or toroidal $(\nabla \times \boldsymbol{b})_\varphi$ components resulted in no noticeable change in the calculated loss fractions. This confirms quantitatively that the drift induced by the vertical component of the magnetic field curvature term, $(\nabla \times \boldsymbol{b})_z$, is indeed the primary driver for guiding-center orbit drift and consequent particle losses in this standard CFQS QA equilibrium. The negative loss rate observed for co-passing particles when the $(\nabla \times \boldsymbol{b})_z$ term is deactivated arises because our particles are initialized throughout the entire simulation space, in-

cluding outside the LCFS. When the dominant $(\nabla\times\boldsymbol{b})_z$ loss mechanism is turned off, the loss of particles from within the LCFS is drastically reduced. Simultaneously, a small fraction of particles that started outside the LCFS can enter the confinement region due to weaker, residual effects or the magnetic topology itself. This combination of sharply reduced internal losses and a small influx of external particles leads to the apparent negative loss rate.

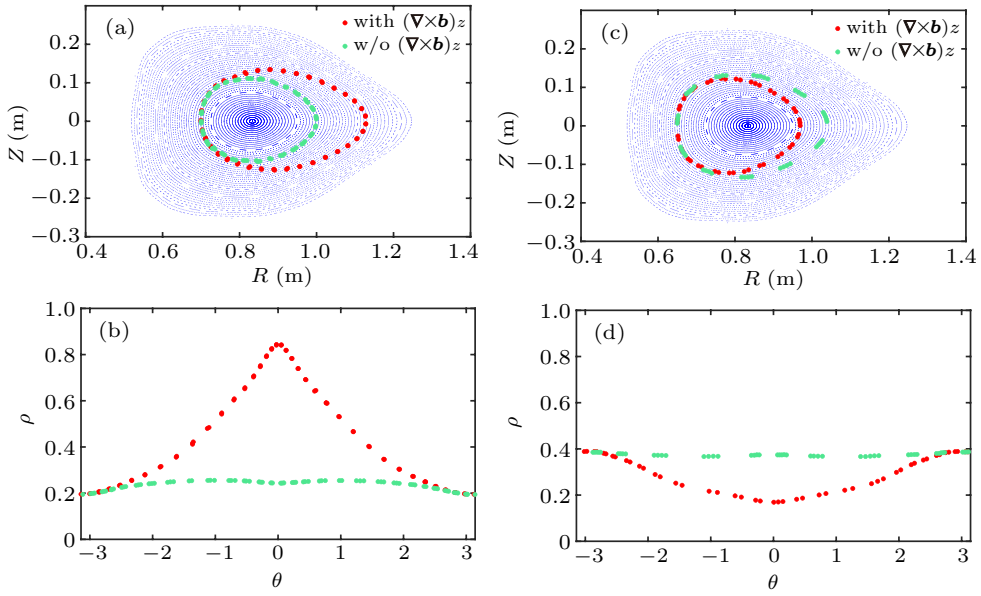


Fig. 3. Effect of deactivating the $(\nabla\times\boldsymbol{b})_z$ term on particle orbits ($v=0.3$): (a) pitch angle $\lambda=-1$ in R–Z space, (b) pitch angle $\lambda=-1$ in θ–ρ space, (c) pitch angle $\lambda=1$ in R–Z space, (d) pitch angle $\lambda=1$ in θ–ρ space.

Table 1. Loss rate calculated from each condition with $v=1.0$.

Loss rate (%)	Initial	W/o $\nabla\times\boldsymbol{b}$	W/o $(\nabla\times\boldsymbol{b})_R$	W/o $(\nabla\times\boldsymbol{b})_z$	W/o $(\nabla\times\boldsymbol{b})_\varphi$
QA co-passing	10.1286	0.1676	15.6991	–1.0215	9.2945
QA counter-passing	76.0169	20.7701	77.8994	22.4018	75.9167

To further investigate the energy dependence of fast particle confinement and quantify the impact of the dominant drift mechanism within the standard CFQS QA configuration, figure 4 presents the calculated loss fraction as a function of the initial normalized particle velocity v ranging from $6\sim1.5$. The figure displays results for both co-passing $(\lambda=1)$ and counter-passing $(\lambda=-1)$ particles. Solid lines represent simulations using the full equations, incorporating all drift effects. Dashed lines show the corresponding loss fractions when the effect associated with the vertical component of the magnetic field curvature term, $(\nabla\times\boldsymbol{b})_z$, is artificially deactivated in the simulation.

Observing the results from the full simulations (solid lines), we see that the loss fraction generally increases with particle velocity for both co- and counter-passing particles. This trend is consistent with the understanding that higher energy particles experience larger guiding-center drifts (as seen in Fig. 2), leading to wider orbit drifts and a higher probability of intersecting the plasma boundary. Typically, counter-passing particles exhibit significantly higher loss fractions than co-passing particles in this configuration due to their net outward drift.

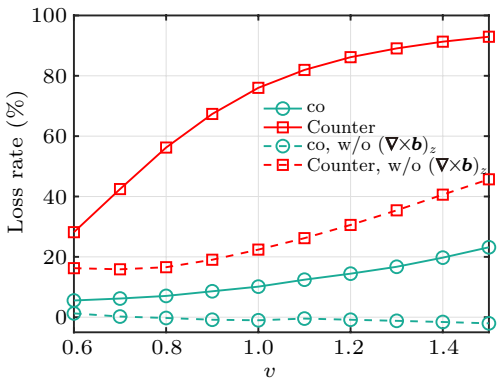


Fig. 4. The loss rate with and without $(\nabla\times\boldsymbol{b})_z$ in QA configuration with different pitch angles $(\lambda=\pm1)$.

The crucial role of the $(\nabla\times\boldsymbol{b})_z$ drift term becomes evident when comparing the solid and dashed lines. Deactivating the $(\nabla\times\boldsymbol{b})_z$ effect (dashed lines) dramatically alters the confinement characteristics. Specifically for co-passing particles, the loss fraction is reduced to nearly zero across the entire velocity range studied. This strongly confirms that the drift motion induced by the $(\nabla\times\boldsymbol{b})_z$ term is the primary loss mechanism for co-passing particles in the standard CFQS QA configuration. For counter-passing particles, turning off the $(\nabla\times\boldsymbol{b})_z$ effect also leads to a significant reduction in the loss fraction compared to the full simulation. However, some resid-

ual losses may persist, especially at higher velocities. This indicates that while the $(\nabla \times \boldsymbol{b})_z$ term is a major contributor to counter-passing particle losses, other drift effects might still contribute to the remaining losses.

In summary, the analysis of loss rate versus velocity clearly demonstrates the detrimental effect of increasing particle energy on confinement and pinpoints the vertical component of the curvature drift, associated with $(\nabla \times \boldsymbol{b})_z$, as the key driver for particle loss, particularly for co-passing particles, in the standard CFQS QA equilibrium.

3.2. Particle orbits in the finite-beta island configuration

We now turn our attention to the particle dynamics within the finite-beta ($\langle\beta\rangle = 0.74\%$) equilibrium configuration. As established in Section 2, this configuration, generated by the HINT code, which features prominent 4/2 magnetic islands. Understanding particle behavior in the presence of such islands is crucial, as they can significantly alter transport and confinement. To specifically investigate the influence of these magnetic islands, we simulated trajectories of fast particles launched near the island with $(R, z, \varphi) = (0.61, \pi/2, 0)$ to focus on its trapping and detrapping effects.

Figure 5 illustrates the trajectories of counter-passing ($\lambda = -1$) particles under these conditions, projected onto the poloidal plane ($\varphi = \pi/2$). The figure presents results for three different initial normalized velocities ($v = 0.02$, 0.04, 0.1). At the lowest velocity (Fig. 5(a)), the particle orbit exhibits clear island-trapped characteristics. The trajectory remains confined within the boundaries of the magnetic island, orbiting around the island's O-point (axis). As the velocity increases (Figs. 5(b) and 5(c)), the particle continues to show characteristics of being trapped by the island potential well. However, a slight net outward radial drift becomes discernible, causing the orbit to shift slightly outwards, consistent with the general behavior of counter-passing particles. Importantly, within this regime of low velocities, the counter-passing particles remain effectively trapped by the island structure and do not transition to standard passing orbits.

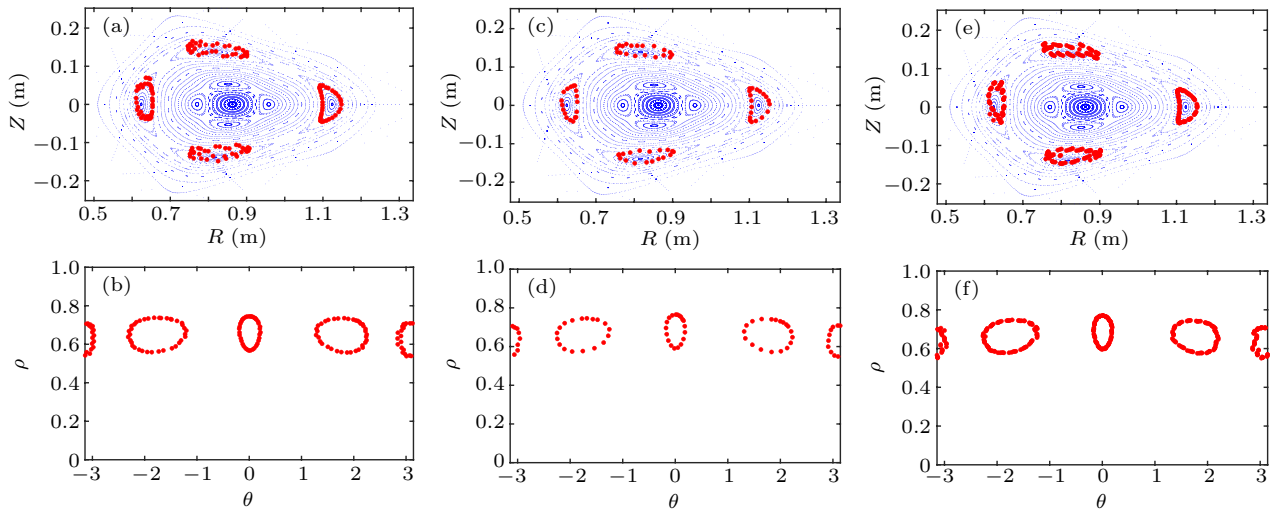


Fig. 5. Counter-passing particle motion at the $\varphi = \pi/2$ section in island configuration: (a) $v = 0.02$ in R–Z space, (b) $v = 0.02$ in θ–ρ space, (c) $v = 0.04$ in R–Z space, (d) $v = 0.04$ in θ–ρ space, (e) $v = 0.1$ in R–Z space, (f) $v = 0.1$ in θ–ρ space.

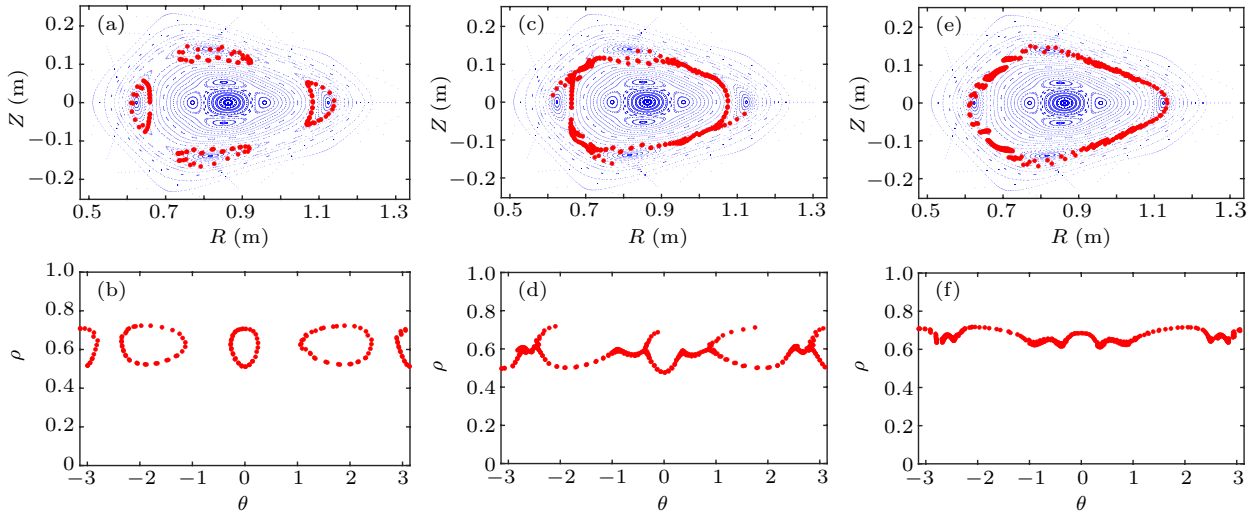


Fig. 6. Co-passing particle motion at the $\varphi = \pi/2$ section in island configuration: (a) $v = 0.02$ in R–Z space, (b) $v = 0.02$ in θ–ρ space, (c) $v = 0.04$ in R–Z space, (d) $v = 0.04$ in θ–ρ space, (e) $v = 0.1$ in R–Z space, (f) $v = 0.1$ in θ–ρ space.

Figure 6 presents the corresponding trajectories for co-passing ($\lambda = 1$) particles launched from the same location within the island, again with increasing initial velocities ($v =$ 0.02, 0.04, 0.1). Like the counter-passing case, at the lowest velocity (Fig. 6(a)), the co-passing particle is initially trapped within the magnetic island.

However, a distinct behavior emerges for co-passing particles as their velocity increases. In Figs. 6(b) and 6(c), we observe that the island's trapping effect weakens with increasing v. The particle trajectories begin to significantly deviate from the simple island-circulating pattern. Notably, these co-passing particles transition from being island-trapped to becoming standard co-passing orbits that circulate toroidally around the magnetic axis. This transition phenomenon was absent for the counter-passing particles in Fig. 5 within the same velocity range. Concurrently with this transition and the increase in velocity, a slight net inward radial drift develops, consistent with the general behavior of co-passing particles.

These initial results highlight the complex interplay between particle energy, pitch angle, and the magnetic island structure. The islands can effectively trap low-energy particles, but this trapping is sensitive to velocity and pitch angle, with co-passing particles showing a transition to passing orbits at lower energies than counter-passing particles seem to require. The slight drifts observed also suggest that even for trapped or orbit-transitioning particles, the underlying drift mechanisms related to ∇B and curvature are still present, although potentially modified by the island topology.

Based on the observations in Figs. 5 and 6, we hypothesized that the drift induced by the $(\boldsymbol{\nabla}\times\boldsymbol{b})_z$ term plays a crucial, yet opposing, role in the island trapping behavior for particles with different pitch angles. Specifically, we suspected that the associated inward drift facilitates the transition of co-passing particles out of the island trap, while the outward drift enhances the trapping of counter-passing particles within the island.

To directly test this hypothesis, we performed simulations analogous to Figure 3, focusing on the velocity $v = 0.1$ where the transition was observed for co-passing particles. Figure 7 compares the particle trajectories calculated with the full equations (red lines) against those where the $(\boldsymbol{\nabla}\times\boldsymbol{b})_z$ effect is deactivated (green lines), for particles launched inside the magnetic island.

The results show that for the counter-passing particle ($\lambda = -1$, Fig. 7(a)), the trajectory calculated with the full equations shows a clear island-trapped orbit. However, when the $(\boldsymbol{\nabla}\times\boldsymbol{b})_z$ term effect (driving outward drift) is removed, the particle is no longer trapped and becomes a passing particle. This demonstrates that the outward drift associated with $(\boldsymbol{\nabla}\times\boldsymbol{b})_z$ is essential for maintaining the trapped state for these counter-passing particles at this velocity. For the co-passing particle ($\lambda = 1$, Fig. 7(b)): With the full equations, the particle exhibits a passing orbit, having already transitioned out of the island trap (consistent with Fig. 6(c)). Remarkably, when the $(\boldsymbol{\nabla}\times\boldsymbol{b})_z$ term effect (driving inward drift) is deactivated, the particle reverts to an island-trapped orbit. This confirms that the inward drift generated by the $(\boldsymbol{\nabla}\times\boldsymbol{b})_z$ term is indeed the key mechanism enabling the co-passing particle to overcome the island's potential barrier and transition to a passing orbit at this velocity.

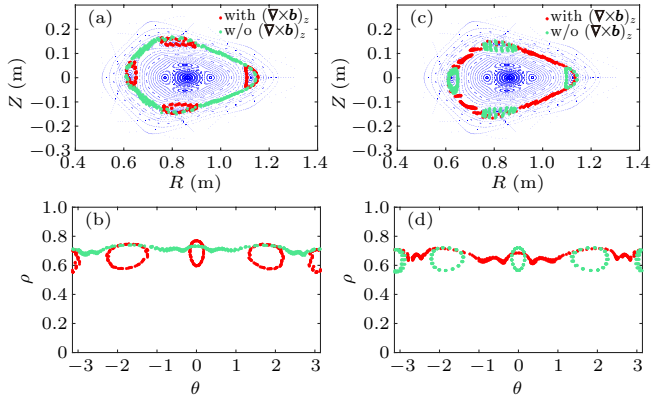


Fig. 7. Effect of deactivating the $(\boldsymbol{\nabla}\times\boldsymbol{b})_z$ term on particle orbits ($v = 0.1$): (a) pitch angle $= -1$ in R–Z space, (b) pitch angle $= -1$ in θ–ρ space, (c) pitch angle $= 1$ in R–Z space, (d) pitch angle $= 1$ in θ–ρ space.

The seemingly counter-intuitive results in Fig. 7, where an outward drift enhances trapping while an inward drift promotes escape, can be explained by the specific topology of the magnetic island. The key is that particle escape from the island trap is not determined by the global drift direction itself, but by whether the particle's orbit is pushed towards the island's 'escape route' — the separatrix region near the magnetic island. For a counter-passing particle (Fig. 7(a)), the outward $(\boldsymbol{\nabla}\times\boldsymbol{b})_z$ drift pushes its orbit away from the inner X-point, pressing it against the outer boundary of the island. This reinforces the trapping, preventing its transition to a passing orbit. Conversely, for a co-passing particle (Fig. 7(c)), the inward $(\boldsymbol{\nabla}\times\boldsymbol{b})_z$ drift steers its orbit directly towards the X-point. This drift provides the necessary 'push' for the particle to access the escape channel, facilitating its transition from a trapped to a standard passing orbit, as observed. Therefore, figure 7 clearly illustrates the differential impact of the $(\boldsymbol{\nabla}\times\boldsymbol{b})_z$ drift term, confirming its role in promoting island escape for co-passing particles (via inward drift) while simultaneously reinforcing island trapping for counter-passing particles (via outward drift) in the finite-beta CFQS configuration.

Finally, the impact of the $(\boldsymbol{\nabla}\times\boldsymbol{b})_z$ term on the overall confinement within the finite-beta island configuration is quantified by examining the loss fraction as a function of initial particle velocity, as shown in Fig. 8. Like the standard QA case (Fig. 4), the results compare the full guiding-center simulation (solid lines) with simulations where the $(\boldsymbol{\nabla}\times\boldsymbol{b})_z$ effect is deactivated (dashed lines) for both co-passing ($\lambda = 1$)

and counter-passing ($\lambda = -1$) particles over the velocity range from 0.6 to 1.5.

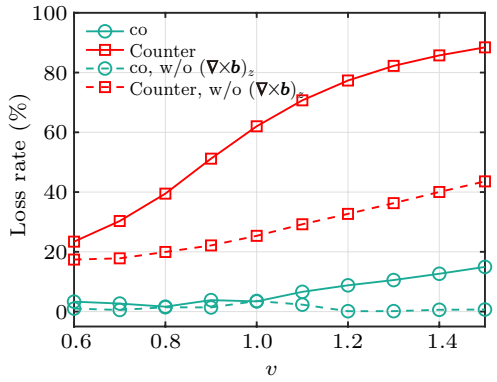


Fig. 8. The loss rate with and without $(\nabla\times\boldsymbol{b})_z$ in island configuration with different pitch angles ($\lambda = \pm 1$).

Consistent with general expectations and the standard QA results, the full simulation (solid lines) shows that counter-passing particles suffer significantly higher losses than co-passing particles, and losses tend to increase with velocity. Deactivating the $(\nabla\times\boldsymbol{b})_z$ (dashed lines) leads to a noticeable reduction in the loss fraction for both particle classes. For co-passing particles, whose loss fraction was already relatively low in the full simulation, removing the $(\nabla\times\boldsymbol{b})_z$ effect decreases the losses further. For counter-passing particles, deactivating this term results in a substantial drop in the loss fraction across the studied velocity range. These results succinctly demonstrate that even in the presence of magnetic islands, the drift associated with the $(\nabla\times\boldsymbol{b})_z$ term remains a key driver contributing significantly to fast particle losses, particularly for counter-passing particles, in this finite-beta CFQS equilibrium.

3.3. Discussion

A deeper comparison between the standard QA (Fig. 4) and finite-beta island (Fig. 8) configurations reveals the complex, dual role of magnetic islands in fast particle confinement, particularly within the collisionless framework of this study where prompt orbit loss is the dominant loss channel.

For co-passing particles, the results are particularly insightful. When all drift effects are active (solid lines), the island configuration paradoxically exhibits a lower net loss rate than the standard QA case. This is not due to permanent trapping, but rather to a temporary trapping of the particle's orbit by the island. In the standard case, the $(\nabla\times\boldsymbol{b})_z$ drift directly causes passing orbits to shift and loss. In the island case, however, the island structure acts as a temporary "safe harbor," disrupting the simple passing trajectory and forcing the particle into a quasi-trapped state. While in this state, the particle is not on a direct loss trajectory. The $(\nabla\times\boldsymbol{b})_z$ drift then acts to facilitate the particle's escape from this temporary state, transitioning it back into a standard passing orbit (as shown in Subsection 3.2), which is once again vulnerable to drift-induced loss. The net loss is lower because the time spent in the island's protective state reduces the overall probability of loss within the simulation time. This protective effect is especially pronounced at lower energies, establishing a clear loss threshold not seen in the standard configuration.

Conversely, when the dominant $(\nabla\times\boldsymbol{b})_z$ drift is deactivated (dashed lines), the comparison isolates the effect of the magnetic topology itself. The island configuration then shows a higher loss rate, attributed to its inherent topological transport channel via the stochastic region, a feature absent in the well-nested standard case.

For counter-passing particles, a different behavior emerges at high energies. The loss rate curves for both configurations (solid red lines) converge. This indicates that for high-energy particles, the powerful outward drift becomes the overwhelmingly dominant loss mechanism, ejecting the particle so rapidly that it cannot significantly interact with the detailed magnetic topology, rendering the differences between the two configurations irrelevant.

In summary, this section presented detailed simulation results on fast particle confinement in two distinct CFQS configurations using the MEGA code. In the standard QA configuration (Subsection 3.1), the vertical component associated with the magnetic field curvature term $(\nabla\times\boldsymbol{b})_z$, was identified as the primary driver for particle orbit drift and losses, especially for co-passing particles. Loss fractions generally increased with particle energy. In the finite-beta configuration featuring magnetic islands (Subsection 3.2), additional complex orbit behaviors emerged, including the trapping of low-energy particles within the island structure. The $(\nabla\times\boldsymbol{b})_z$ drift term was found to play a crucial role in modulating this trapping effect, facilitating island escape for co-passing particles while reinforcing trapping for counter-passing particles. Despite the presence of islands, this drift term remained a significant contributor to overall particle losses in the finite-beta equilibrium, particularly for counter-passing particles.

4. Conclusions

This study employed the MEGA code to investigate and compare the confinement characteristics of fast particles in two distinct magnetic equilibria of the CFQS stellarator: (i) the standard quasi-axisymmetric (QA) configuration, and (ii) a finite-beta ($\langle\beta\rangle = 0.74\%$) configuration featuring prominent magnetic islands, generated using the HINT code. By analyzing particle trajectories and quantitatively assessing losses, including the identification of dominant drift mechanisms through selective deactivation of terms in the drift kinetic equations, the following key conclusions have been drawn:

In the standard CFQS QA configuration:

(i) The guiding-center drift associated with the vertical component of the magnetic field curvature, represented by

the $(\nabla \times \boldsymbol{b})_z$ term, was definitively identified as the primary mechanism driving orbit drift and subsequent fast particle losses.

(ii) Deactivating this $(\nabla \times \boldsymbol{b})_z$ term effect virtually eliminated losses for co-passing particles and significantly reduced losses for counter-passing particles across the studied energy range, confirming its dominant role.

(iii) Consistent with drift physics, particle loss fractions generally increase with energy, and counter-passing particles exhibit significantly higher losses than co-passing particles due to their net outward drift.

In the finite-beta ($\langle\beta\rangle = 0.74\%$) configuration with magnetic islands:

(I) The presence of magnetic islands introduces complex orbit topologies, notably the trapping of low-velocity particles within the island structure.

(II) The $(\nabla \times \boldsymbol{b})_z$ drift term plays a crucial role in modulating this island trapping behavior. Its associated inward drift facilitates the transition of co-passing particles from island-trapped to passing orbits as energy increases, while its outward drift reinforces the trapping of counter-passing particles within the island.

(III) Despite the presence of islands and associated trapping effects at low energy, the $(\nabla \times \boldsymbol{b})_z$ drift remains a significant contributor to overall fast particle losses in the finite-beta equilibrium, particularly for counter-passing particles at higher energies.

Overall, the $(\nabla \times \boldsymbol{b})_z$ term effect indeed has a crucial effect on particle confinement. It is noteworthy that a comparison between the loss fractions presented in Fig. 4 (standard QA) and figure 8 (high-beta island) indicates that the overall fast particle losses do not increase dramatically in the finite-beta equilibrium, despite the presence of magnetic islands. This suggests that the CFQS configuration possesses a degree of robustness in maintaining reasonable magnetic surface quality and confinement characteristics even at this finite beta. Therefore, in subsequent NBI experiments, it is necessary to select appropriate injection angles and energy levels to minimize fast particle losses. Our results, which pinpoint the $(\nabla \times \boldsymbol{b})_z$ drift as the dominant loss mechanism, offer specific guidance for this selection. Given that counter-passing particles exhibit significantly higher losses, NBI strategies should prioritize creating co-passing particles. This implies that a tangential co-injection geometry would be strongly preferable to minimize prompt losses. Furthermore, an on-axis or near-tangential injection path would be optimal to keep particle orbits well-centered and away from the plasma boundary. These considerations suggest that a high-confinement scenario in CFQS would be best achieved with an on-axis, co-tangential NBI system. It is important to emphasize that the present study utilized static magnetic equilibrium fields without including MHD effects. Finally, it is crucial to emphasize that our conclusions regarding the dominance of the $(\nabla \times \boldsymbol{b})_z$ drift apply specifically to the passing particle population ($|\lambda| = 1$) investigated here. This focus was chosen to isolate the curvature drift mechanism. For particles with mixed pitch angles ($v_\perp > 0$), the gradient-B drift would also contribute significantly to transport, and the interplay between these drift mechanisms could lead to different loss dynamics. A comprehensive study of confinement across the full pitch-angle space remains a critical topic for future investigation.

Acknowledgements

The authors would like to thank Prof. Y. Todo for the MEGA code. Project supported by the National MCF Energy Research and Development Program of China (Grant No. 2024YFE03170001), the National Natural Science Foundation of China (Grant No. U22A20262), the Fundamental Research Funds for the Central Universities (Grant No. 2682024ZTPY035), the Science and Technology Plan Project in Sichuan Province of China (Grant No. 2022JDJQ0036), NIFS International Collaborations with Overseas Laboratories (Grant No. UFEX105), NIFS Promotion of Magnetic Confinement Research using Helical Devices in Asia (Grant No. URSX108), the NIFS General Collaboration Project (Grant Nos. NIFS18KBAP041, NIFS20KBAP067, NIFS20KBAE001, NIFS22KIPH009, NIFS22KIPH011, and NIFS22KIEE001), and 'PLADyS', JSPS Core-to-Core Program, A. Advanced Research Networks.

References

[1] Okamura S, Murakami S, Shimizu A, Isobe M, Nishimura S, Suzuki C, Matsuoka K, Nomura I, Minami T and Iguchi H 2000 *J. Plasma Fusion Res. SERIES*, Vol. 3 **73**
[2] Xu Y 2016 *Matter Radiat. Extremes* **1** 192
[3] Okamura S, Matsuoka K, Nishimura S, Isobe M, Nomura I, Suzuki C, Shimizu A, Murakami S, Nakajima N, Yokoyama M, Fujisawa A, Ida K, Itoh K, Merkel P, Drevlak M, Zille R, Gori S and Nührenberg J 2001 *Nucl. Fusion* **41** 1865
[4] Matsuoka K, Okamura S, Nishimura S, Isobe M, Suzuki C, Shimizu A, Tanaka N, Hasegawa M, Naito H, Urata K, Suzuki Y and Tsukamoto T 2004 *Fusion Sci. Technol.* **46** 378
[5] Okamura S, Matsuoka K, Nishimura S, Isobe M, Suzuki C, Shimizu A, Ida K, Fujisawa A, Murakami S, Yokoyama M, Itoh K, Hayashi T, Nakajima N, Sugama H, Wakatani M, Nakamura Y and Cooper W A 2004 *Nucl. Fusion* **44** 575
[6] Reiman A, Fu G, Hirshman S, *et al.* 1999 *Plasma Phys. Control. Fusion* **41** B273
[7] Neilson G H, Reiman A H, Zarnstorff M C, *et al.* 2000 *Phys. Plasmas* **7** 1911
[8] Zarnstorff M C, Berry L A, Brooks A, *et al.* 2001 *Plasma Phys. Control. Fusion* **43** A237
[9] Henneberg S A, Drevlak M, Nührenberg C, Beidler C D, Turkin Y, Loizu J and Helander P 2019 *Nucl. Fusion* **59** 026014
[10] Liu H, Shimizu A, Isobe M, Okamura S, Nishimura S, Suzuki C, Xu Y, Zhang X, Liu B, Huang J, Wang X, Liu H, Tang C, Yin D, Wan Y and CFQS team 2018 *Plasma Fusion Res.* **13** 3405067
[11] Liu H, Shimizu A, Xu Y, Okamura S, Kinoshita S, Isobe M, Li Y, Xiong G, Wang X, Huang J, Cheng J, Liu H, Zhang X, Yin D, Wang Y, Murase T, Nakagawa S and Tang C 2021 *Nucl. Fusion* **61** 016014

[12] Shimizu A, Liu H, Isobe M, Okamura S, Nishimura S, Suzuki C, Xu Y, Zhang X, Liu B, Huang J, Wang X, Liu H and Tang C 2018 *Plasma Fusion Res.* **13** 3403123
[13] Shimizu A, Kinoshita S, Isobe M, *et al.* 2022 *Nucl. Fusion* **62** 016010
[14] Isobe M, Shimizu A, Liu H, Liu H, Xiong G, Yin D, Ogawa K, Yoshimura Y, Nakata M, Kinoshita S, Okamura S, Tang C and Xu Y 2019 *Plasma Fusion Res.* **14** 3402074
[15] Kinoshita S, Shimizu A, Okamura S, Isobe M, Xiong G, Liu H and Xu Y 2019 *Plasma Fusion Res.* **14** 3405097
[16] Yoshimura Y, Kanda M, Yanai R, Shimizu A, Kinoshita S, Isobe M, Okamura S, Ogawa K, Takahashi H, Murase T, Nakagawa S, Tanoue H, Liu H and Xu Y 2022 *Plasma Fusion Res.* **17** 2402039
[17] Wang X Q, Xu Y, Shimizu A, Isobe M, Okamura S, Todo Y, Wang H, Liu H F, Huang J, Zhang X, Liu H, Cheng J and Tang C J 2021 *Nucl. Fusion* **61** 036021
[18] Paul E J, Bhattacharjee A, Landreman M, Alex D, Velasco J L and Nies R 2022 *Nucl. Fusion* **62** 126054
[19] Su C Y, Chen S Y, Liu H F, Mou M L, Guo W P and Tang C J 2020 *AIP Adv.* **10** 015004
[20] Yang L, Liu H, Shimizu A, Xu Y, Wang X, Liu H, Tang C, Li Y, Liu J, Luo Y, Xiong G, Su C, Kinoshita S, Isobe M, Okamura S, Huang J, Zhang X, Yin D and Wan Y 2020 *Europhys. Lett.* **132** 35001
[21] Todo Y and Sato T 1998 *Phys. Plasmas* **5** 1321
[22] Todo Y 2006 *Phys. Plasmas* **13** 082503
[23] Todo Y, Berk H L and Breizman B N 2010 *Nucl. Fusion* **50** 084016
[24] Todo Y, Shinohara K, Takechi M and Ishikawa M 2005 *Phys. Plasmas* **12** 012503
[25] Zou Y, Chan V S, Todo Y, Ma R, Xue M, Zhang X, Zhu Y and Chen W 2025 *Nucl. Fusion* **65** 026034
[26] Gogoleva A, Tribaldos V, Reynolds-Barredo J M and Beidler C D 2020 *Nucl. Fusion* **60** 056009
[27] Suzuki Y, Nakajima N, Watanabe K, Nakamura Y and Hayashi T 2006 *Nucl. Fusion* **46** L19